Brazilian Journal
of Chemical
Engineering

ISSN 0104-6632
Printed in Brazil
www.abeq.org.br/bjche

Vol. 33, No. 02, pp. 347 - 360, April - June, 2016
dx.doi.org/10.1590/0104-6632.20160332s20150011

3D COMPOSITIONAL RESERVOIR SIMULATION IN CONJUNCTION WITH UNSTRUCTURED GRIDS

A. L. S. Araújo[1], B. R. B. Fernandes[2], E. P. Drumond Filho[2], R. M. Araujo[2], I. C. M. Lima[2], A. D. R. Gonçalves[2], F. Marcondes[3*] and K. Sepehrnoori[4]

[1]Federal Institute of Education, Science and Technology of Ceará, Fortaleza - CE, Brazil.
[2]Laboratory of Computational Fluid Dynamics, Federal University of Ceará, Fortaleza - CE, Brazil.
[3]Department of Metallurgy and Materials Science and Engineering,
Federal University of Ceará, Fortaleza - CE, Brazil.
[*]E-mail: marcondes@ufc.br
[4]Center for Petroleum and Geosystems Engineering, The University of Texas at Austin, USA.

(Submitted: January 7, 2015 ; Revised: April 6, 2015 ; Accepted: May 24, 2015)

Abstract - In the last decade, unstructured grids have been a very important step in the development of petroleum reservoir simulators. In fact, the so-called third generation simulators are based on Perpendicular Bisection (PEBI) unstructured grids. Nevertheless, the use of PEBI grids is not very general when full anisotropic reservoirs are modeled. Another possibility is the use of the Element based Finite Volume Method (EbFVM). This approach has been tested for several reservoir types and in principle has no limitation in application. In this paper, we implement this approach in an in-house simulator called UTCOMP using four element types: hexahedron, tetrahedron, prism, and pyramid. UTCOMP is a compositional, multiphase/multicomponent simulator based on an Implicit Pressure Explicit Composition (IMPEC) approach designed to handle several hydrocarbon recovery processes. All properties, except permeability and porosity, are evaluated in each grid vertex. In this work, four case studies were selected to evaluate the implementation, two of them involving irregular geometries. Results are shown in terms of oil and gas rates and saturated gas field.
Keywords: EbFVM; Compositional reservoir simulation; IMPEC approach; Unstructured grids.

INTRODUCTION

Proper petroleum reservoir modeling requires the correct evaluation of several important geometric parameters, such as sealing faults, fractures, irregular reservoir shapes, and deviated wells. Although simple to use, conventional Cartesian grids, commonly employed in petroleum reservoir simulation, cannot produce accurate modeling of most of the aforementioned geometric features. The first application of unstructured grids in the petroleum reservoir area were carried out by Forsyth (1990), Fung *et al*. (1991), and Gottardi *et al*. (1992). The above-mentioned authors conducted a 2D discretization of material balance equations using linear triangular elements. The approach developed in these works was called the Control Volume Finite Element Method (CVFEM). The multicomponent/multiphase approximate equations were obtained from the single-phase equations multiplied by phase mobilities. Verma and Aziz (2002) and Edwards (2002) developed the multipoint-flux approach. In this method, all physical properties are stored in each vertex of the grid, including the porosity and the absolute permeability tensor. This method was implemented for triangular and quadrilateral elements. One drawback of this

*To whom correspondence should be addressed

approach is the necessity to solve a local linear system in order to maintain the flux continuity. This issue is raised by the storage of permeability in each vertex of the grid. Using the Element based Finite-Volume Method (EbFVM), as presented in this paper, and storing a permeability tensor for each element overcomes this problem. Furthermore, fully heterogeneous and anisotropic reservoirs can also be handled using this approach.

Several studies have been conducted in order to further develop and enhance the CVFEM method. Cordazzo (2004) and Cordazzo *et al*. (2004) applied the ideas of Raw (1985) and Baliga and Patankar (1983) to simulate waterflooding problems. Concerning the final governing equations, this method is very similar to the CVFEM. The resulting approach was called the Element-based Finite Volume Method (EbFVM), which is a more suitable denomination, since it borrows the flexibility of the finite-element method to discretize the domain, but keeps the conservative idea from the finite-volume method. The main difference between the CVFEM approach commonly used in petroleum reservoir simulation and the EbFVM technique lies in the assumption of multiphase/multi-component flow of the EbFVM approach in order to obtain the approximate equations, while the CVFEM first obtains the approximate equations for single phase flow and then multiplies the resulting equations by the mobilities in order to obtain the approximate equations for multiphase flow. Later, Paluszny *et al*. (2007) presented a full tridimensional discretization for hexahedron, tetrahedron, prism, and pyramid elements in conjunction with water flooding problems. Marcondes and Sepehrnoori (2010) and Marcondes *et al*. (2013) applied the EbFVM to 2D and 3D isothermal, compositional problems using a fully implicit approach. Santos *et al*. (2013) applied the EbFVM to the solution of 3D compositional miscible gas flooding with dispersion, once again associated with the fully implicit approach. These works demonstrated that more accurate solutions can be obtained with the EbFVM compared to Cartesian grids. Fernandes *et al*. (2013) investigated several interpolation functions for the solution of compositional problems for 2D reservoirs in conjunction with the EbFVM approach. Marcondes *et al*. (2015) implemented EbFVM to 2D and 3D thermal, compositional reservoir simulator in conjunction with a fully implicit approach.

This work presents an investigation of the EbFVM method for the solution of isothermal, multicomponent/multiphase flows in 3D reservoirs using four element types: hexahedron, tetrahedron, prism and pyramid in conjunction with an IMPEC (Implicit Pressure Explicit Composition) approach. The porosity and permeability tensors are constant throughout each element. All remaining properties are evaluated at the vertices of each element, defining a cell-vertex approach. The method was implemented in the UTCOMP simulator, developed at the Center of Petroleum and Geosystems Engineering at The University of Texas at Austin for handling several compositional, multiphase/multicomponent recovery processes. To the best of our knowledge, this is the first time that the EbFVM in conjunction with hexahedrons, tetrahedrons, prisms, and pyramids is implemented and tested for compositional reservoir simulation based on an IMPEC approach.

GOVERNING EQUATIONS

According to Wang *et al*. (1997), in order to describe an isothermal, multiphase/multicomponent flow in a porous medium, three types of equations are required: the material balance for all components, the phase equilibrium equations, and the equations for constraining phase saturations and component concentrations.

The material balance equation for each component is given by

$$\frac{1}{V_b}\frac{\partial N_i}{\partial t} - \vec{\nabla}\cdot\sum_{j=1}^{n_p}\left[\xi_j\lambda_j x_{ij}\bar{\bar{k}}\cdot\vec{\nabla}\Phi_j\right] - \frac{q_i}{V_b} = 0 \quad \text{for } i = 1,2,\cdots,n_c \,, \tag{1}$$

where N_i is the number of moles of the i-th component, ξ_j, λ_j are respectively, the molar density and molar mobility of the j-th phase, x_{ij} is the mole fraction of the i-th component in the j-th phase, q_i is the molar rate of the i-th component, V_b is bulk volume, $\bar{\bar{k}}$ is the absolute permeability tensor, and Φ_j is the phase potential of the j-th phase which is given by

$$\Phi_j = P_j - \gamma_j D + P_{cjr} \,, \tag{2}$$

where P_j is the pressure of the j-th phase, P_{cjr} represents the capillary pressure between phases j and r, γ_j is the specific gravity of the j-th phase, and D is the reservoir depth which is positive in the downward direction. In UTCOMP, the oil phase is the reference phase.

Following the material balance, the phase equilibrium calculation must be performed. The phase equilibrium calculations are necessary to determinate the

number and composition of all phases, satisfying three conditions. First, the molar-balance equation has to be considered. Next, the chemical potentials for each component must be the same for every phase. The last condition is the minimization of the Gibbs free energy. The first partial derivate of the total Gibbs free energy for the independent variables results in the equality of all component fugacities throughout all phases, which can be stated, considering oil as the reference phase (*r*), as

$$f_i^j - f_i^r = 0 \quad (i = 1,2,\cdots,n_c;\ j = 3,\cdots,n_p;\ r = 2). \tag{3}$$

Note that the water phase is not included in the phase equilibrium calculations.

The phase composition constraints and the equation for determining the phase amounts for both hydrocarbon phases are, respectively, given by

$$\sum_{i=1}^{n_c} x_{ij} - 1 = 0 \qquad (j = 1,2,\cdots,n_p), \tag{4}$$

$$\sum_{i=1}^{n_c} \frac{z_i\left(K_i - 1\right)}{1 + v\left(K_i - 1\right)} = 0. \tag{5}$$

In Eq. (5), K_i stands for the equilibrium ratio for each component, z_i is the overall mole fraction, and v represents the gas mole fraction in the absence of water.

The last equation to be obtained is the pressure equation. The UTCOMP simulator is based on an IMPEC (Implicit Pressure, Explicit Composition) approach. In this formulation, the pressure is solved implicitly, while the conservations, Equation (1), are evaluated explicitly. In each grid block, the pressure is obtained from the assumption that the pore volume is completely filled with the total volume of fluid

$$V_t(P,\vec{N}) = V_p(P), \tag{6}$$

where the pore volume (V_p) is a function only of the pressure, while the total fluid volume (V_t) is a function of pressure and the total number of moles of each component. Differentiating each side of Eq. (6) with respect to their independent variables, the pressure equation (Ács *et al*., 1985; Chang, 1990) is obtained as follows:

$$\begin{aligned} &\frac{1}{V_b}\left(V_p^0 c_f - \frac{\partial V_t}{\partial P}\right)\left(\frac{\partial P}{\partial t}\right) - \sum_{i=1}^{n_c+1} \bar{V}_{ti}\vec{\nabla} \\ &\cdot\sum_{j=1}^{n_p} \lambda_{rj}\xi_j x_{ij}\bar{\bar{k}}\cdot\vec{\nabla}P = \sum_{i=1}^{n_c+1} \bar{V}_{ti}\vec{\nabla} \\ &\cdot\sum_{j=1}^{n_p} \lambda_{rj}\xi_j x_{ij}\bar{\bar{k}}\cdot\left(\vec{\nabla}P_{cjo} - \gamma_j\vec{\nabla}D\right) + \frac{1}{V_b}\sum_{i=1}^{n_c+1} \bar{V}_{ti}q_i\,, \end{aligned} \tag{7}$$

where $\bar{V}_{ti}$ represents the derivative of total fluid volume related to N_i.

APROXIMATE EQUATIONS

The EbFVM method is characterized by dividing each element into sub-elements according to the number of vertices. Conservation equations, Eqs. (1) and (7), are integrated over each sub-element. After the division of the elements into sub-elements, we call them sub-control volumes. The material balance is established for every sub-control volume, and then, the control volume balance equation is built by adding the contributions of every sub-control volume that shares the same vertex.

Each element type has a certain sub-control volume division based on the number of vertices. Figure 1 shows the division for each of the four elements investigated in this work, according to the number of vertices. From Figure 1, it is possible to infer that each sub-control volume for hexahedron, prism, and tetrahedron elements is composed of three quadrilateral integration surfaces. The exception is the pyramid element, whose sub-control volumes associated with the base have three triangular integration surfaces and the one associated with the apex has four quadrilateral integration surfaces. In Figure 1, the numbers that reside inside a circle refer to the integration surface and the others refer to the vertices.

Integrating Eq. (1) in time and over each sub-control volume, followed by the application of the Gauss theorem for the advective term, we obtain:

$$\begin{aligned} &\int_{V,t} \frac{1}{V_b}\frac{\partial N_i}{\partial t}dVdt - \int_{A,t}\sum_{j=1}^{n_p} \xi_j\, x_{ij}\,\lambda_j\bar{\bar{k}}\cdot\vec{\nabla}\Phi_j\cdot d\vec{A}\,dt \\ &-\int_{V,t}\frac{q_i}{V_b}dVdt = 0\ ;\ i = 1,2,..,n_{c+1}\,. \end{aligned} \tag{8}$$

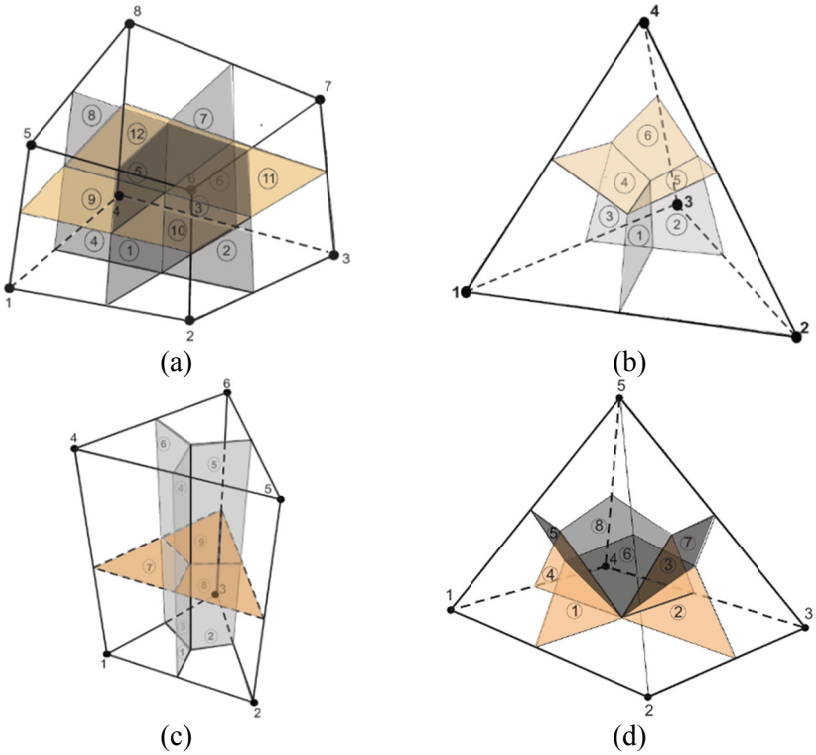

Figure 1: Sub-control volumes for the four element types: (a) hexahedron, (b) tetrahedron, (c) prism, and (d) pyramid (Marcondes *et al*., 2015).

In order to evaluate the volume, area and gradient in Eq. (8), it is necessary to define the shape functions for each element type. The shape functions for hexahedron, tetrahedron, prism, and pyramid elements are, respectively, defined as follows:

$$
\begin{aligned}
N_1(s,t,p)&=\frac{(1+s)(1-t)(1+p)}{8};\\
N_2(s,t,p)&=\frac{(1+s)(1-t)(1-p)}{8}\\
N_3(s,t,p)&=\frac{(1-s)(1-t)(1-p)}{8};\\
N_4(s,t,p)&=\frac{(1-s)(1-t)(1+p)}{8}\\
N_5(s,t,p)&=\frac{(1+s)(1+t)(1+p)}{8};\\
N_6(s,t,p)&=\frac{(1+s)(1+t)(1-p)}{8}\\
N_7(s,t,p)&=\frac{(1-s)(1+t)(1-p)}{8};\\
N_8(s,t,p)&=\frac{(1-s)(1+t)(1+p)}{8},
\end{aligned}
\tag{9}
$$

$$
\begin{aligned}
&N_1(s,t,p)=1-s-t-p\ ;\ N_2(s,t,p)=s\\
&N_3(s,t,p)=t\ ;\ N_4(s,t,p)=p,
\end{aligned}
\tag{10}
$$

$$
\begin{aligned}
&N_1(s,t,p)=(1-s-t)(1-p)\ ;\ N_2(s,t,p)=s(1-p)\\
&N_3(s,t,p)=t(1-p)\ ;\ N_4(s,t,p)=p(1-s-t)\\
&N_5(s,t,p)=sp\ ;\ N_6(s,t,p)=tp,
\end{aligned}
\tag{11}
$$

$$
\begin{aligned}
N_1(s,t,p)&=\frac{1}{4}[(1-s)(1-t)-p+stp/(1-p)]\\
N_2(s,t,p)&=\frac{1}{4}[(1+s)(1-t)-p-stp/(1-p)]\\
N_3(s,t,p)&=\frac{1}{4}[(1+s)(1+t)-p-stp/(1-p)]\\
N_4(s,t,p)&=\frac{1}{4}[(1-s)(1+t)-p-stp/(1-p)]\\
N_5(s,t,p)&=p\,.
\end{aligned}
\tag{12}
$$

In the shape function equations presented above, s, t, and p are the coordinates in a local reference frame, defined in each element. This local frame allows all elements to be treated equally, regardless of how distorted an element is in the global x, y, and z system. Since we employ the shape functions to evaluate any physical property or geometry position inside each element, these elements are called isoparametric elements (Hughes, 1987):

$$x(s,t,p)=\sum_{i=1}^{Nv} N_i\, x_i \;\; ; \;\; y(s,t,p)=\sum_{i=1}^{Nv} N_i\, y_i \;\; ;$$
$$z(s,t,p)=\sum_{i=1}^{Nv} N_i\, z_i \;\; ; \;\; \Phi_j(s,t,p)=\sum_{i=1}^{Nv} N_i\, \Phi_{ji}. \tag{13}$$

In Eq. (13), N_v and N_i denote the number of vertices and the shape functions of each element, respectively. From Eq. (13), the gradient of phase potential can be written as

$$\frac{\partial \Phi_j}{\partial x}=\sum_{i=1}^{Nv}\frac{\partial N_i}{\partial x}\Phi_{ji} \;; \frac{\partial \Phi_j}{\partial y}=\sum_{i=1}^{Nv}\frac{\partial N_i}{\partial y}\Phi_{ji} \;; \frac{\partial \Phi_j}{\partial z} = \sum_{i=1}^{Nv}\frac{\partial N_i}{\partial z}\Phi_{ji}. \tag{14}$$

The shape function derivatives required for computing the gradients in Eq. (14) are given by:

$$\begin{aligned}
\frac{\partial N_i}{\partial x} &= \frac{1}{\det(J_t)}\left(\frac{\partial y}{\partial t}\frac{\partial z}{\partial p}-\frac{\partial y}{\partial p}\frac{\partial z}{\partial t}\right)\frac{\partial N_i}{\partial s} \\
&\quad -\frac{1}{\det(J_t)}\left(\frac{\partial y}{\partial s}\frac{\partial z}{\partial p}-\frac{\partial y}{\partial p}\frac{\partial z}{\partial s}\right)\frac{\partial N_i}{\partial t} \\
&\quad +\frac{1}{\det(J_t)}\left(\frac{\partial y}{\partial s}\frac{\partial z}{\partial t}-\frac{\partial y}{\partial t}\frac{\partial z}{\partial s}\right)\frac{\partial N_i}{\partial p} \\
\frac{\partial N_i}{\partial y} &= -\frac{1}{\det(J_t)}\left(\frac{\partial x}{\partial t}\frac{\partial z}{\partial p}-\frac{\partial x}{\partial p}\frac{\partial z}{\partial t}\right)\frac{\partial N_i}{\partial s} \\
&\quad +\frac{1}{\det(J_t)}\left(\frac{\partial x}{\partial s}\frac{\partial z}{\partial p}-\frac{\partial x}{\partial p}\frac{\partial z}{\partial s}\right)\frac{\partial N_i}{\partial t} \\
&\quad -\frac{1}{\det(J_t)}\left(\frac{\partial x}{\partial s}\frac{\partial z}{\partial t}-\frac{\partial x}{\partial t}\frac{\partial z}{\partial s}\right)\frac{\partial N_i}{\partial p} \\
\frac{\partial N_i}{\partial z} &= \frac{1}{\det(J_t)}\left(\frac{\partial x}{\partial t}\frac{\partial y}{\partial p}-\frac{\partial x}{\partial p}\frac{\partial y}{\partial t}\right)\frac{\partial N_i}{\partial s} \\
&\quad -\frac{1}{\det(J_t)}\left(\frac{\partial x}{\partial s}\frac{\partial y}{\partial p}-\frac{\partial x}{\partial p}\frac{\partial y}{\partial s}\right)\frac{\partial N_i}{\partial t} \\
&\quad +\frac{1}{\det(J_t)}\left(\frac{\partial x}{\partial s}\frac{\partial z}{\partial t}-\frac{\partial x}{\partial t}\frac{\partial y}{\partial s}\right)\frac{\partial N_i}{\partial p},
\end{aligned} \tag{15}$$

where $\det(J_t)$ is the Jacobian of the transformation and is given for all sub-control volumes by:

$$\begin{aligned}
\det(J_t) &= \frac{\partial x}{\partial s}\left(\frac{\partial y}{\partial t}\frac{\partial z}{\partial p}-\frac{\partial y}{\partial p}\frac{\partial z}{\partial t}\right) \\
&\quad -\frac{\partial x}{\partial t}\left(\frac{\partial y}{\partial s}\frac{\partial z}{\partial p}-\frac{\partial y}{\partial p}\frac{\partial z}{\partial s}\right) \\
&\quad +\frac{\partial x}{\partial p}\left(\frac{\partial y}{\partial s}\frac{\partial z}{\partial t}-\frac{\partial y}{\partial t}\frac{\partial z}{\partial s}\right).
\end{aligned} \tag{16}$$

The sub-control volumes for the hexahedron, tetrahedron, prism, and pyramid elements are given, respectively, by Eqs. (17) through (20), and the area for quadrilateral integration surfaces is given by Eq. (21).

$$V_{scv,i}=\det(J_t), \tag{17}$$

$$V_{scv,i}=\det(J_t)/6, \tag{18}$$

$$V_{scv,i}=\det(J_t)/12, \tag{19}$$

$$V_{scv,i}=\begin{cases} 2\det(J_t)/9 & for \quad i=1,...,4 \;(base) \\ 4\det(J_t)/9 & for \quad i=5 \;(apex) \end{cases}, \tag{20}$$

$$\begin{aligned}
d\vec{A} &= \left(\frac{\partial y}{\partial m}\frac{\partial z}{\partial n}-\frac{\partial y}{\partial n}\frac{\partial z}{\partial m}\right)dm\,dn\,\hat{i} \\
&\quad -\left(\frac{\partial x}{\partial n}\frac{\partial z}{\partial m}-\frac{\partial x}{\partial m}\frac{\partial z}{\partial n}\right)dm\,dn\,\hat{j} \\
&\quad +\left(\frac{\partial x}{\partial m}\frac{\partial y}{\partial n}-\frac{\partial x}{\partial n}\frac{\partial y}{\partial m}\right)dm\,dn\,\hat{k},
\end{aligned} \tag{21}$$

where m and n in Eq. (21) represent the local system *s*, *t*, or *p*. The computation of the integrated surface area for the remaining element types is similar. Equations (17) - (20) and Eq. (21) are used to evaluate, respectively, the accumulation term (*Acc*) and the advective flux (*F*).

$$Acc_{m,i}=\frac{V_{scv_{m,i}}}{V_{b,m}}\left(\left(\frac{N_m}{\Delta t}\right)_i^{n+1}-\left(\frac{N_m}{\Delta t}\right)_i^{n}\right); \quad m=1,N_v \;;\; i=1,..,n_c+1, \tag{22}$$

$$\begin{aligned}
F_{m,i} &= \int_A \sum_{j=1}^{n_p}\left(\xi_j\, x_{ij}\, \lambda_j \bar{\bar{k}}\cdot\vec{\nabla}\Phi_j\right)\cdot d\vec{A} \\
&= \sum_{ip=1}^{3}\left(\sum_{j=1}^{n_p}\xi_j^n\, x_{ij}^n\, \lambda_j^n k_{nl}\left.\frac{\partial \Phi_j}{\partial x_l}\right|_{ip} A_n\right);
\end{aligned} \tag{23}$$

$$m=1,N_v \;;\; n,l=1,...,3; i=1,n_c+1.$$

From Eq. (23), it is possible to infer that it is necessary to calculate molar densities, mole fractions, and molar mobilities at each one of the interfaces of each sub-control volume. Also, it is important to note that the aforementioned properties are evaluated at the previous time step (superscript n); the superscript 'n+1' denotes the current time-step. It is also important to indicate that, for the potential term in Eq. (23), only the pressure is evaluated implicitly, while the other terms (capillary pressure and gravitational terms) are evaluated explicitly. In order to evaluate the mentioned properties, an upwind scheme is used. Considering the integration point 1 of Fig 1, for all the elements, the mobility is calculated as:

$$\begin{aligned} \lambda_{jip1} &= \lambda_{j2} \quad if \quad \overline{\overline{k}} \cdot \vec{\nabla}\Phi_j \cdot d\vec{A}\Big|_{ip1} \leq 0 \\ \lambda_{jip1} &= \lambda_{j1} \quad if \quad \overline{\overline{k}} \cdot \vec{\nabla}\Phi_j \cdot d\vec{A}\Big|_{ip1} > 0. \end{aligned} \tag{24}$$

Inserting Eqs. (22) and (23) in Eq. (8), the final equation for each sub-control volume is given by

$$Acc_{m,i} + F_{m,i} + q_i = 0 \; ; \; m = 1,...,N_v \; ; \; i = 1,...,n_c + 1. \tag{25}$$

Eq. (25) represents the material balance for each sub-control volume. The equations for each control-volume are assembled from the contribution of all sub-control volumes that share the same vertex. Further details about this procedure can be found in Marcondes and Sepehrnoori (2010) and Marcondes *et al*. (2013). A similar procedure realized for the molar balance equation needs to be performed for the pressure equation.

RESULTS AND DISCUSSION

In this section, results for four case studies are presented. The two first case studies are designed to validate the current implementation with the Cartesian implementation of the UTCOMP simulator, and the other two case studies are designed to demonstrate the ability of the EbFVM approach to handle irregular geometries. It is important to emphasize that the Cartesian implementation of UTCOMP simulator has been validated using many analytical solutions as well as several commercial simulators (Chang, 1990; Fernandes *et al*., 2013). The first case is a CO_2 injection characterized by three hydrocarbon components in a quarter-of-five-spot configuration. The reservoir data, components and composition data, and binary coefficients are shown in Tables 1 through 3, respectively. For all grid configurations investigated in this work, red arrows denote producer wells, while blue arrows denote injecting wells.

Table 1: Reservoir data for Case 1.

Property	Value
Length, width, and thickness	170.69 m, 170.69 m, and 30.48 m
Porosity	0.30
Initial Water Saturation	0.25
Initial Pressure	20.65 MPa
Permeability in X, Y, and Z directions	1.974×10^{-13} m^2, 1.974×10^{-13} m^2, and 1.974×10^{-14} m^2
Formation Temperature	299.82 K
Gas Injection Rate	5.66×10^2 m^3/d
Producer's Bottom Hole Pressure	20.65 MPa

Table 2: Fluid composition data for Case 1.

Component	Initial Reservoir Composition	Injection Fluid Composition
CO_2	0.0100	0.9500
C_1	0.1900	0.0500
n-C_{16}	0.8000	-

Table 3: Binary interaction coefficients for Case 1.

Component	CO_2	C_1	n-C_{16}
CO_2	-	0.12	0.12
C_1	0.12	-	-
n-C_{16}	0.12	-	-

The volumetric rates of oil and gas obtained with all the four elements investigated and the refined Cartesian grid are presented in Figure 2. From this figure, it is possible to infer that all four elements produce results that are in good agreement with the ones obtained with the refined Cartesian grid. Also, the number of volumes for all elements used is much smaller than the ones used by the Cartesian grid, demonstrating that, at least for this case study, the EbFVM approach is much more accurate than the Cartesian grid. Accuracy can be explained based on the larger Jacobian stencil of the unstructured grid compared to the convention seven bandwidth diagonals of the Cartesian grid.

In order to visualize the pyramid mesh, Figure 3 shows a x-y plane cut through the apex of one pyramid element.

Figure 4 presents the saturation gas field at 500 days for all elements tested and for the Cartesian grid. From this figure, once again it is possible to conclude that very good sharp fronts were obtained with all elements and these results are in good agreement with the refined Cartesian mesh.

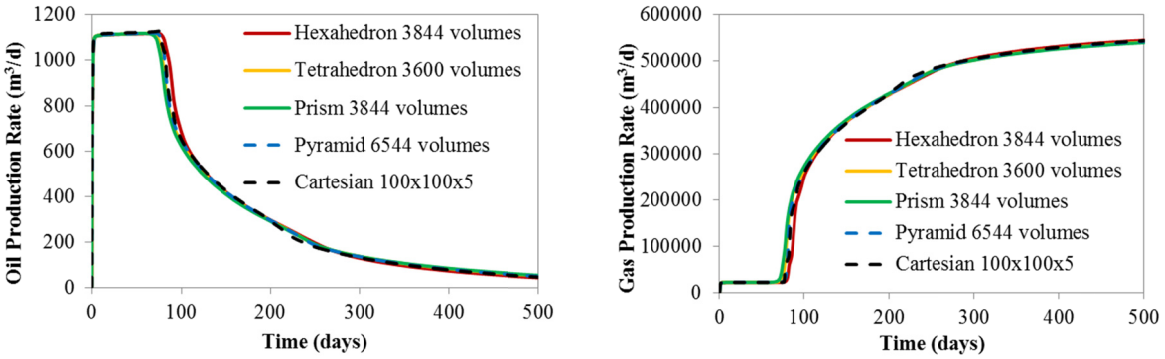

(a) (b)

Figure 2: Volumetric rates - Case 1: a) Oil and b) Gas.

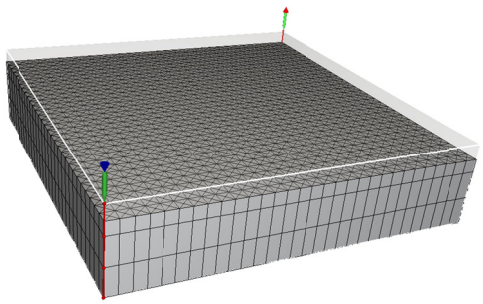

Figure 3: Aerial view of the cut plane of the pyramid mesh.

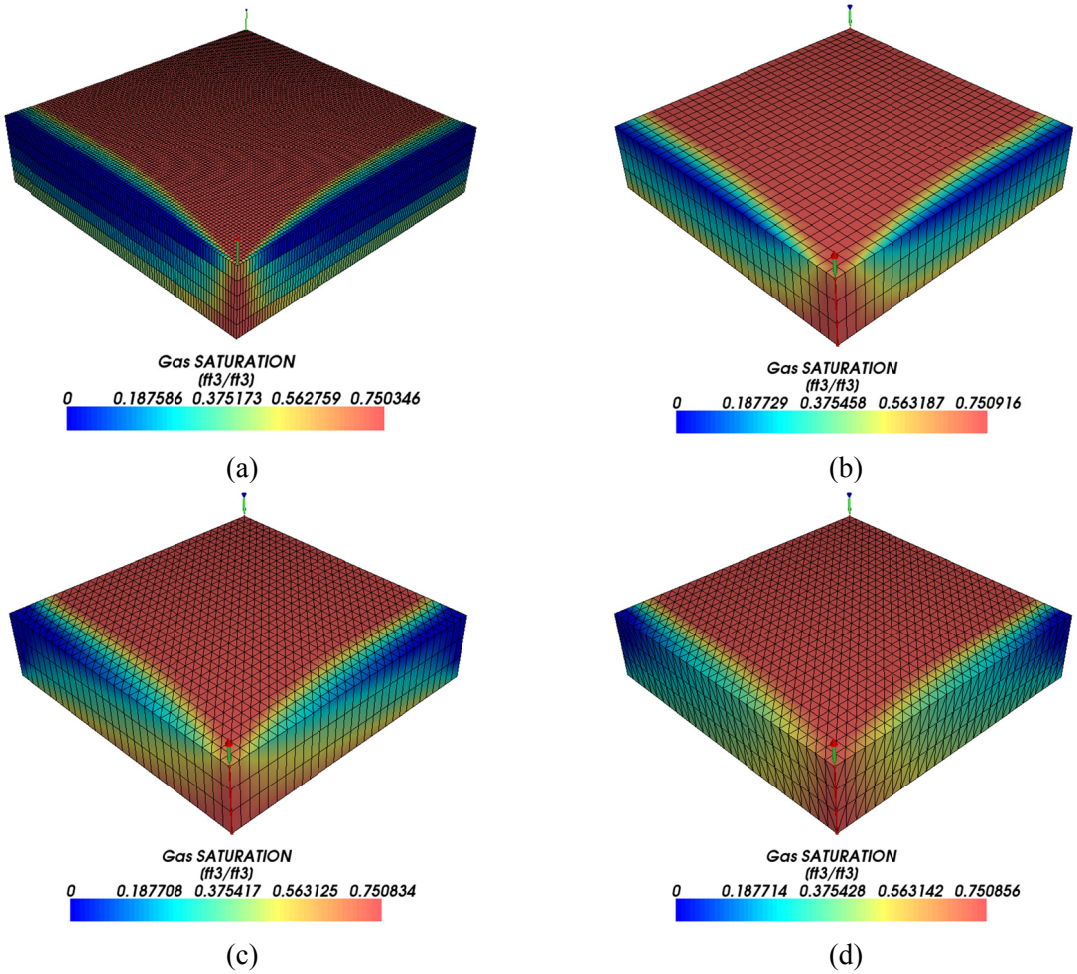

(a) (b)

(c) (d)

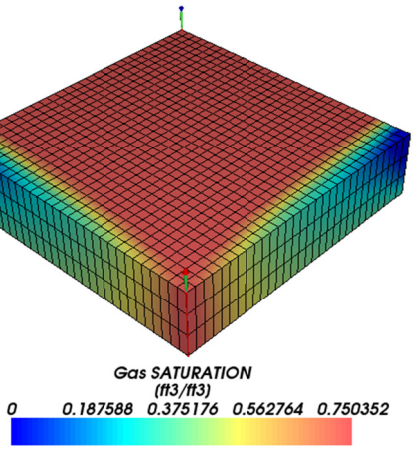

(e)

Figure 4: Gas saturation at 500 days for Case 1. (a) Cartesian; (b) Hexahedron; (c) Prism; (d) Tetrahedron and (e) Pyramid.

The second case study again refers to a CO_2 injection problem in a quarter-of-five spot and is characterized with same fluid of case study 1. The difference is that the binary interaction coefficients are all set to zero, which in turn makes the injected fluid completely miscible with the oil in-place.

Figure 5 shows the comparison between the Cartesian grid and the four element types, for Case 2, in terms of oil and gas production rates. The results presented in Fig. 5 show a satisfactory match for all elements and the Cartesian grid.

The CO_2 overall mole fraction field at 500 days is shown in Figure 6. From the results presented, it is possible to observe a good agreement between the EbFVM for all elements and the Cartesian grid.

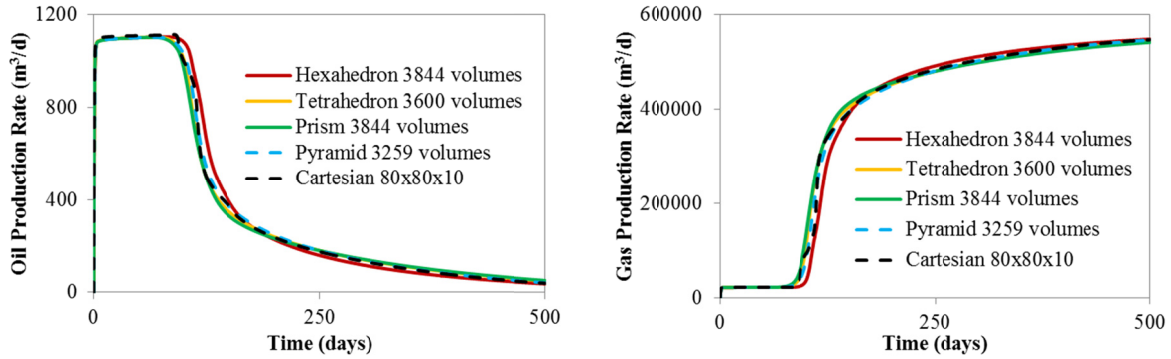

(a) (b)

Figure 5: Volumetric rates - Case 2: a) Oil and b) Gas.

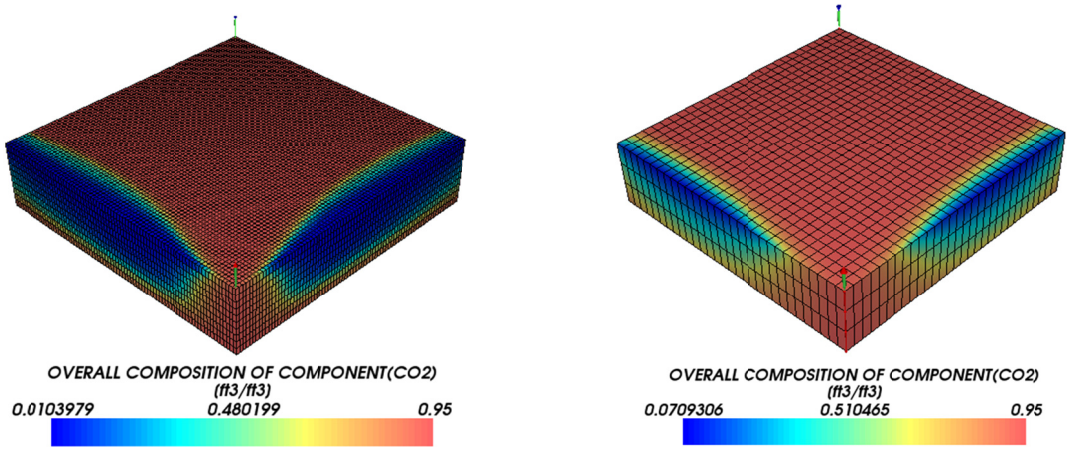

(a) (b)

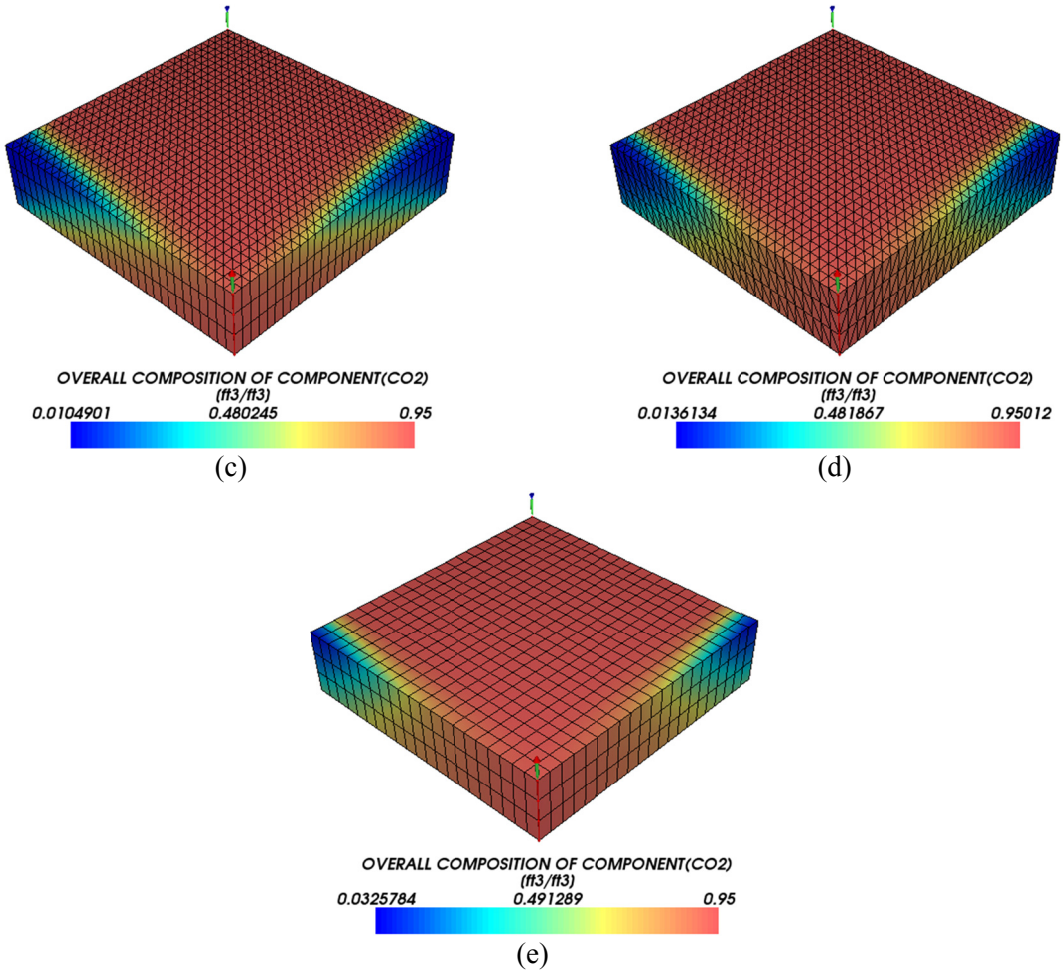

Figure 6: CO_2 overall mole fraction fields for Case 2 at 500 days. (a) Cartesian; (b) Hexahedron; (c) Prism; (d) Tetrahedron and (e) Pyramid.

The third case study again refers to a gas flooding problem in an irregular reservoir characterized by seven hydrocarbon components. The 3D irregular reservoir is shown in Figure 7. Just to have an idea of the reservoir dimensions, the sizes in Figure 7 are shown in feet. Two grid configurations are presented in Figure 7; Figure 7a shows a grid composed of only hexahedron elements, and Figure 7b shows a hybrid mesh composed of hexahedron, tetrahedron, and pyramids elements.

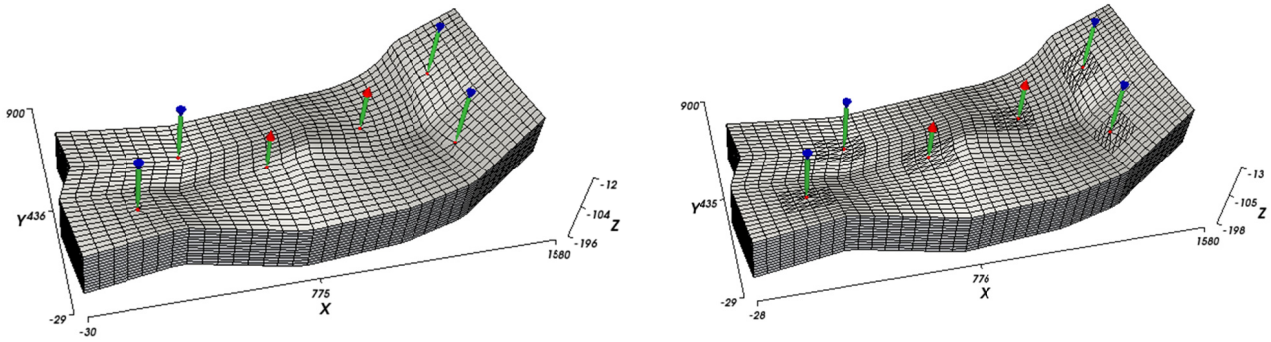

Figure 7: Grid configurations used for Case 3. (a) Hexahedron grid (14896 vertices; 12987 elements) and (b) hybrid grid (19928 vertices; 14352 tetrahedrons; 12688 hexahedrons; 7800 pyramids).

The reservoir and fluid composition data are given in Tables 4 and 5, respectively.

Table 4: Reservoir data for Case 3.

Property	Value
Porosity	0.163
Initial Water Saturation	0.25
Initial Pressure	19.65 MPa
Permeability in X, Y, and Z directions	$1.974x10^{-13}$ m^2, $1.974x10^{-13}$ m^2, and $1.974x10^{-14}$ m^2
Formation Temperature	400 K
Gas Injection Rate	$14.16x10^3$ m^3/d
Producer's Bottom Hole Pressure	19.65 MPa

Table 5: Fluid composition data for Case 3.

Component	Initial Reservoir Composition	Injection Fluid Composition
CO_2	0.0077	0.96
C_1	0.2025	0.01
C_2-C_3	0.1180	0.01
C_4-C_6	0.1484	0.01
C_7-C_{14}	0.2863	0.01
C_{15}-C_{24}	0.1490	-
C_{25+}	0.0881	-

Figure 8 shows the total oil and gas volumetric rates from the two producers obtained in conjunction with the hexahedron and hybrid (hexahedron, tetrahedron and prism elements) refined grids. From this figure, it is possible to see a good agreement between the results obtained with the two different grid configurations.

Figure 9 presents the gas saturation field at two simulated times (100 days; 280 days) obtained with the hexahedron and hybrid grids shown in Figure 7. Although, the grid configurations are completely different from each other, the gas saturation fields presented in Fig. 9 are in good agreement. Also, good resolution fronts with small numerical dispersion were observed.

The fourth case study is a mixed fluid (liquid and gas) injection characterized by five hydrocarbon components in a 3D irregular grid. Figure 10 presents two grid configurations: a hexagonal and a hybrid grid. Just to have an idea of the reservoir dimensions, the sizes in Fig. 10 are shown in feet. In terms of the geometric model, this case is different from Case 3, since there is an internal hole that mimics a region of small permeability tensor. If a Cartesian mesh is used to model such an area, inactive cells should be used. Using the EbFVM approach, no additional calculation is necessary.

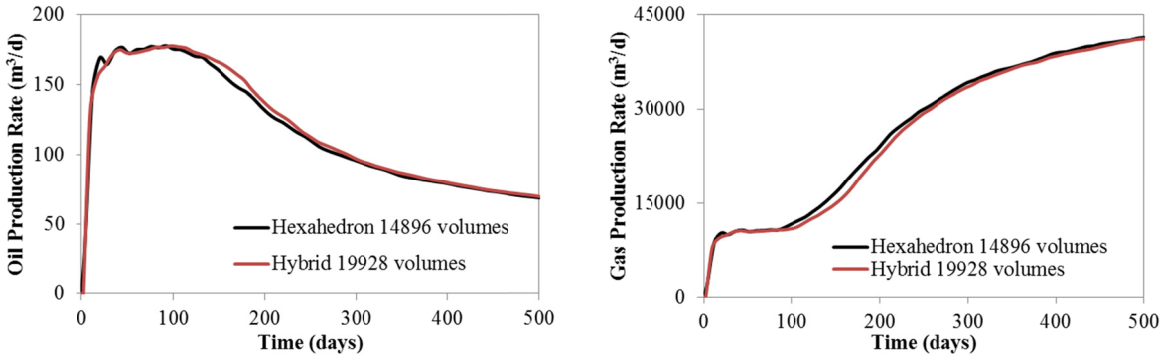

(a) (b)

Figure 8: Volumetric rates for Case 3. a) Oil and b) Gas

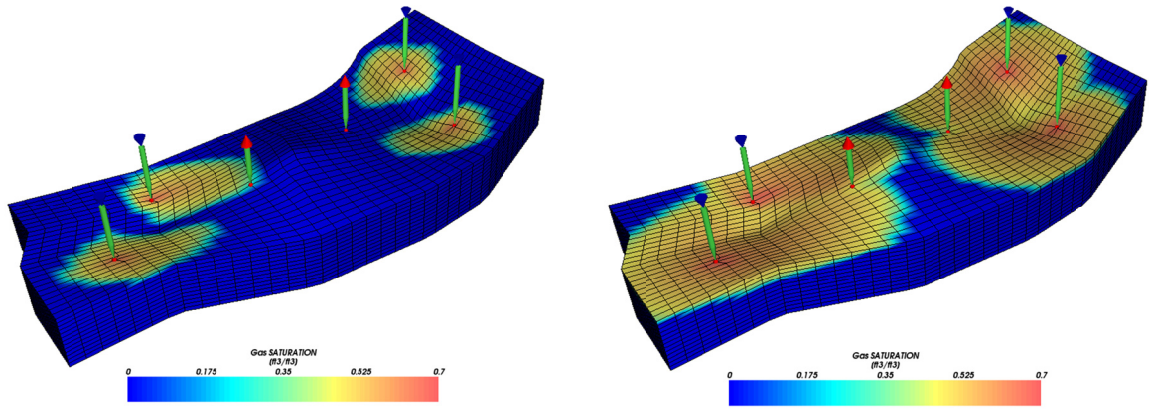

(a) (b)

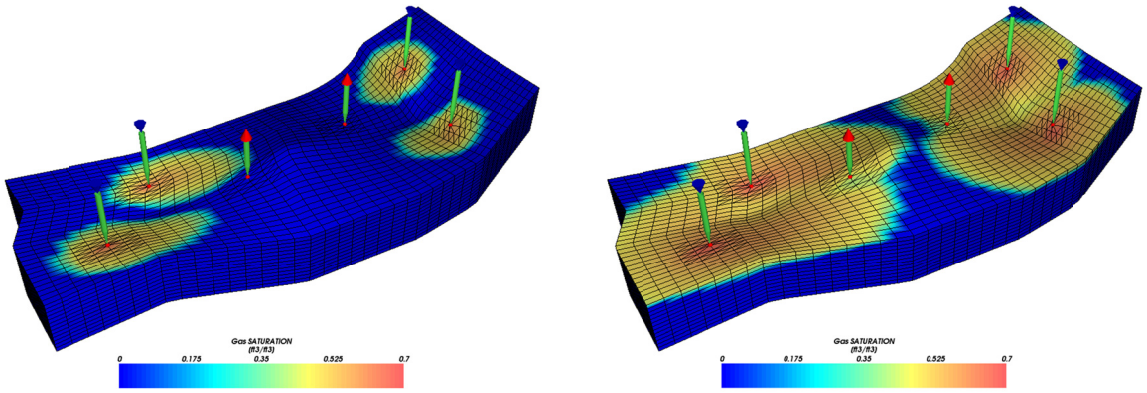

(c) (d)

Figure 9: Gas saturation fields for Case 3. Hexahedron: a) 100 days, b) 280 days. Hybrid: c) 100 days, d) 280 days.

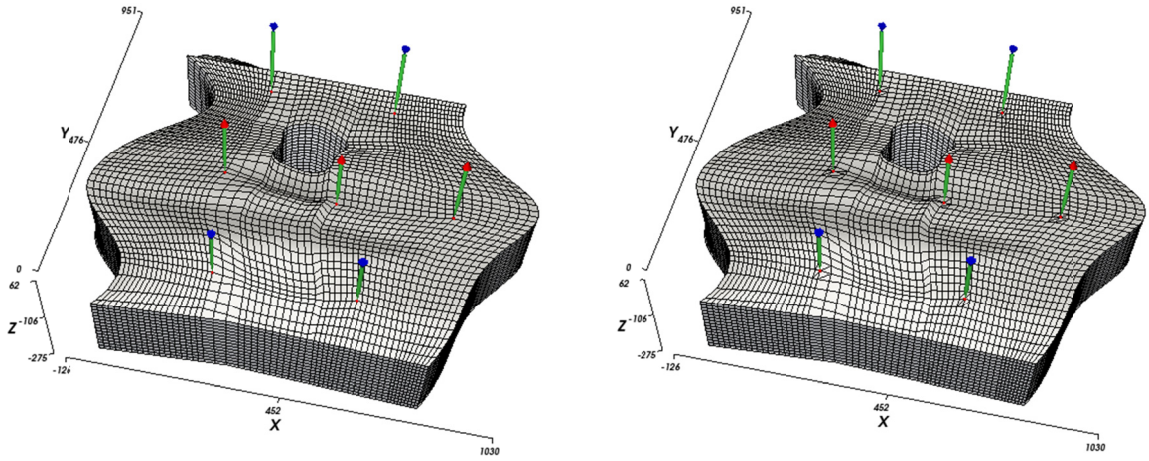

(a) (b)

Figure 10: Grid configurations used for Case 4. (a) Hexahedron grid (41392 vertices; 36975 elements) and (b) hybrid grid (42232 vertices; 4200 tetrahedrons;35715 hexahedrons; 4200 pyramids).

The reservoir and fluid composition information are shown in Tables 6 and Table 7, respectively.

Figure 11 presents the oil and gas rates in conjunction with the hexahedron and hybrid grids. From this figure, is possible to observe a very good match between the two grid configurations investigated.

Table 6: Reservoir data for Case 4.

Property	Value
Porosity	0.35
Initial Water Saturation	0.17
Initial Pressure	10.34 MPa
Permeability in all directions	$9.869 \times 10^{-15} m^2$
Formation Temperature	344.26 K
Gas Injection Rate	28.32×10^3 m^3/d
Producer's Bottom Hole Pressure	8.96 MPa

Table 7: Fluid composition data for Case 4.

Component	Initial Reservoir Composition	Injection Fluid Composition
C_1	0.5000	0.7700
C_3	0.0300	0.2000
C_6	0.0700	0.0100
C_{10}	0.2000	0.0100
C_{15}	0.1500	0.0050
C_{20}	0.0500	0.0050

The gas saturation fields at 200 and 1000 days are presented in Figure 12. Once again, an excellent gas saturation front is observed with both grid configurations.

In order to visualize the hybrid grid, a cut plane passing through an injection well and a production well is shown in Figure 13. From this figure, it is possible to see the gas saturation profile, as well as the hybrid grid around the wells.

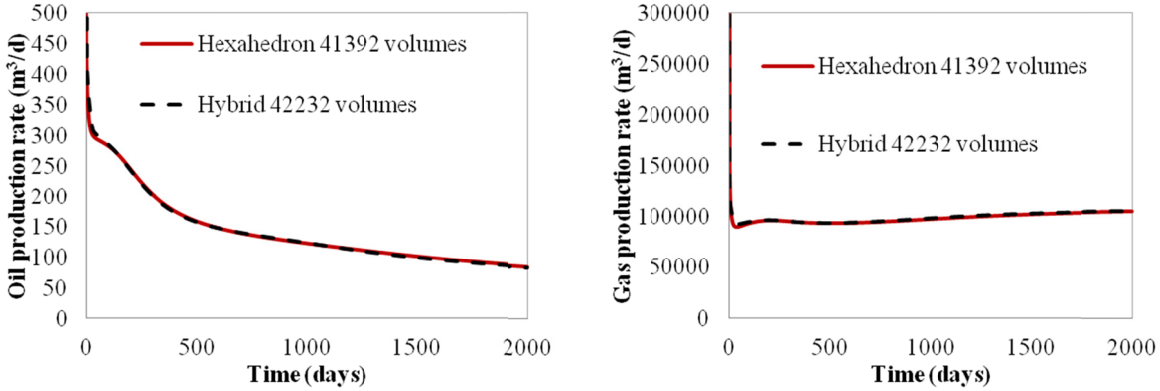

(a) (b)

Figure 11: Volumetric rates for Case 4. a) Oil and b) Gas.

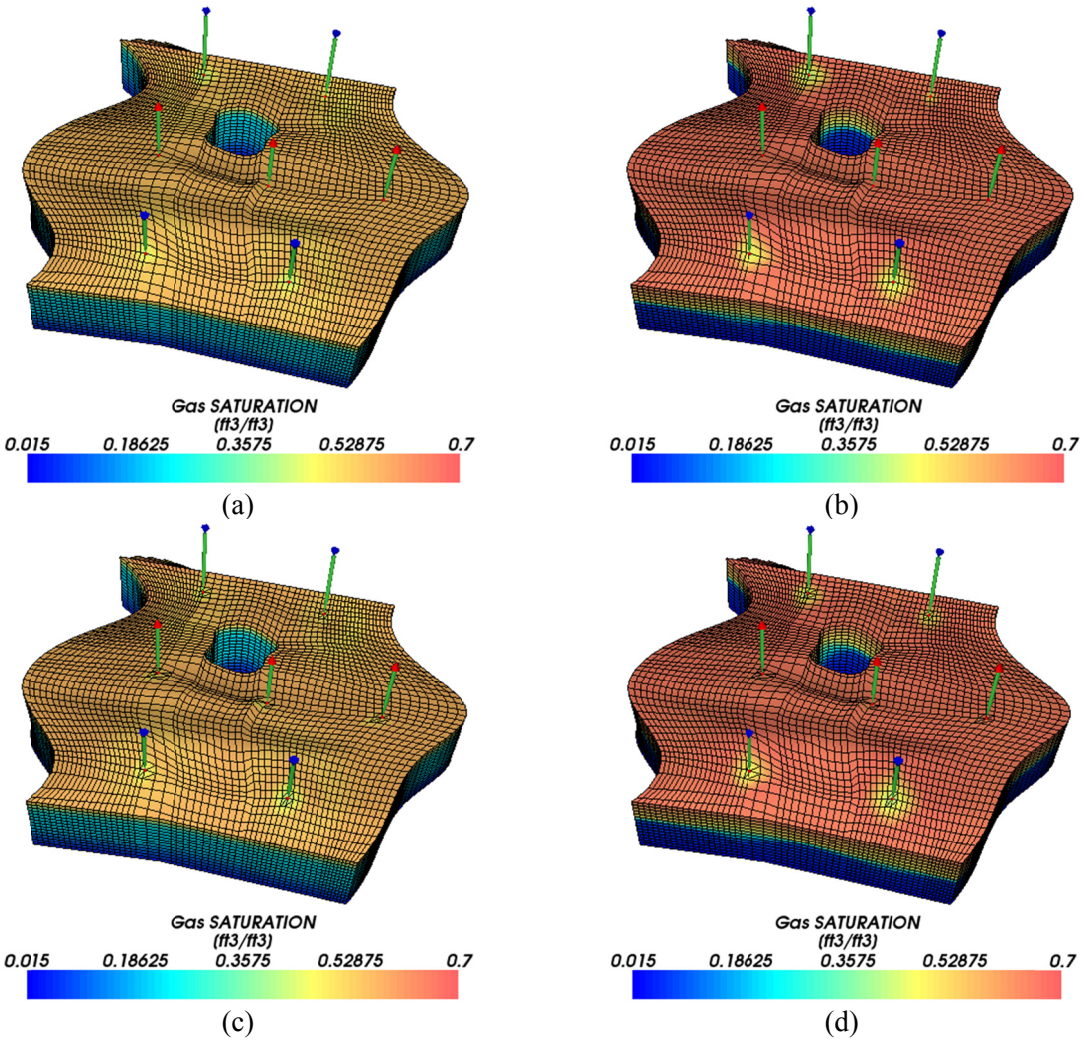

(a) (b)

(c) (d)

Figure 12: Gas saturation fields for Case 4. Hexahedron: a) 200 days, b) 1000 days. Hybrid: c) 200 days, d) 1000 days.

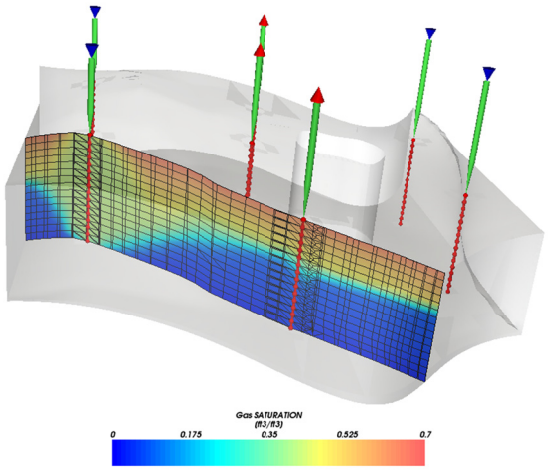

Figure 13: Cut plane through wells - gas saturation in 1000 days.

CONCLUSIONS

This work presents the implementation of an EbFVM formulation using unstructured grids for tridimensional compositional reservoir simulation in conjunction with an IMPEC approach. The method was applied using four element types: hexahedron, tetrahedron, prism, and pyramid. Four different case studies are presented in order to validate and show the flexibility and the accuracy of the EbFVM approach compared to the commonly used Cartesian grids. From the results obtained, it is possible to conclude that EbFVM can be an excellent methodology to handle the important geometric parameters of reservoirs with a high level of accuracy. The investigation in terms of robustness and performance of this approach was not performed in this work, but will be done in the future.

NOMENCLATURE

A	Area (m^2)
Acc	Accumulation term of the material balance (mol/d)
c_f	Rock compressibility (Pa^{-1})
F	Advective flux term of the material balance (mol/d)
f	Fractionary flow or fugacity for the equilibrium constraint
g	Gravity (m/d^2)
J	Mole flux transported by dispersion (mol/m^2 d)
K	Equilibrium ratio
$\overline{\overline{K}}$	Absolute permeability tensor (m^2)
k_r	Relative permeability
N	Number of moles (mol) or shape function
n_c	Number of components
n_p	Number of phases
P	Pressure (Pa)
q	Well mole rate (mol/d)
S	Saturation
t	Time (s)
V_b	Bulk volume (m^3)
V_p	Pore volume (m^3)
V_t	Total fluid volume (m^3)
$\overline{V}_{ti}$	Total fluid partial molar volume (m^3/mol)
$\overline{V}_{\ell i}$	Phase partial molar volume (m^3/mol)
x	Phase mole fraction
z	Overall mole fraction

Greek Letters

γ	Specific gravity (Pa/m)
ξ	Mole density (mol/m^3)
ϕ	Porosity
λ	Phase mobility (Pa^{-1} d^{-1})
Φ	Hydraulic potential (Pa)
μ	Viscosity (Pa d)
ν	Mole fraction in the absence of water

Superscripts

n	Previous time step level
$n+1$	New time step level

Subscripts

i	Control volume
j	Phase
k	Component
r	Reference phase
t	Total

ACKNOWLEDGMENTS

The authors would like to acknowledge PETROBRAS S/A Company for the financial support for this work. Also, the authors would like to thank ESSS Company for providing Kraken® for pre and post-processing the results. Finally, Francisco Marcondes would like to acknowledge the CNPq (the National

Council for Scientific and Technological Development of Brazil) for its financial support through grant No. 305415/2012-3.

REFERENCES

Ács, G., Doleschall, S. and Farkas, E., General purpose compositional model. SPE Journal, 25, p. 543-553 (1985).

Baliga, B. R. and Patankar, S. V., A control volume finite-element method for two-dimensional fluid flow and heat transfer. Numerical Heat Transfer, 6(3), p. 245-261 (1983).

Chang, Y.-B., Development and application of an equation of state compositional simulator. PhD Thesis, The University of Texas at Austin (1990).

Cordazzo, J., Maliska, C. R, Silva, A. F. C., Hurtado, F. S. V., The negative transmissibility issue when using CVFEM in petroleum reservoir simulation - 1. Theory. The 10th Brazilian Congress of Thermal Sciences and Engineering, Rio de Janeiro, Brazil, 29 Nov. 03, Dec (2004).

Cordazzo, J., Maliska, C. R., Silva, A. F. C, Hurtado, F. S. V., The negative transmissibility issue when using CVFEM in petroleum reservoir simulation - 2. Results. The 10th Brazilian Congress of Thermal Sciences and Engineering, Rio de Janeiro, Brazil, 29 Nov – 03 Dec (2004).

Cordazzo, J., An element based conservative scheme using unstructured grids for reservoir simulation. The SPE Annual Technical Conference and Exhibition, Houston, USA, 26-29 Sept (2004).

Edwards, M. G., Unstructured, control-volume distributed, full-tensor finite-volume schemes with flow based grids. Computational Geosciences, 6(3-4) p. 433-452 (2002).

Fernandes, B. R. B., Marcondes, F., Sepehrnoori, K., Investigation of several interpolation functions for unstructured meshes in conjunction with compositional reservoir simulation. Numerical Heat Transfer Part A: Applications, 64(12), p. 974-993 (2013).

Forsyth, P. A., A Control-Volume, Finite-Element Method for Local Mesh Refinement in Thermal Reservoir Simulation. SPE Reservoir Engineering 1990, 5(4), p. 561-566 (1990).

Fung, L. S., Hiebert, A. D., Nghiem, L., Reservoir simulation with a control-volume finite-element method. The 11th SPE Symposium on Reservoir Simulation, Anaheim, USA, 17-20 Feb (1991).

Gottardi, G., Dall´Olio, D., A control-volume finite-element model for simulating oil-water reservoirs. Journal of Petroleum Science and Engineering, 8(1), p. 29-41 (1992).

Hughes, T. J. R., The Finite Element Method, Linear Static and Dynamic Finite Element Analysis. New Jersey, Prentice Hall (1987).

Marcondes, F., Santos, L. O. S., Varavei, A., Sepehrnoori, K., A 3D hybrid element-based finite-volume method for heterogeneous and anisotropic compositional reservoir simulation. Journal of Petroleum Science & Engineering, 108, p. 342-351 (2013).

Marcondes, F., Sepehrnoori, K., An element-based finite-volume method approach for heterogeneous and anisotropic compositional reservoir simulation. Journal of Petroleum Science & Engineering, 73(1-2), p. 99-106 (2010).

Marcondes, F., Varavei, A., Sepehrnoori, K., An EOS-based numerical simulation of thermal recovery process using unstructured meshes. Brazilian Journal of Chemical Engineering, 32(1), 247-258 (2015).

Paluszny, A., Matthäi, S. K., Hohmeyer, M., Hybrid finite element-finite volume discretization of complex geologic structures and a new simulation workflow demonstrated on fractured rocks. Geofluids, 7(2), p. 186-208 (2007).

Raw, M., A new control volume based finite element procedure for the numerical solution of the fluid flow and scalar transport equations. PhD Thesis, University of Waterloo (1985).

Santos, L. O. S., Marcondes, F., Sepehrnoori, K., A 3D compositional miscible gas flooding simulator with dispersion using element-based finite-volume method. Journal of Petroleum Science & Engineering, 112, p. 61-68 (2013).

Verma, S., Aziz, K., A control volume scheme for flexible grids in reservoir simulation. The Reservoir Simulation Symposium, Dallas, USA, 8-11 Jun (1997).

Wang, P., Yotov, I., Wheeler, M., Arbogast, T., Dawson, C., Parashar, M., Sepehrnoori, K., A new generation EOS compositional reservoir simulator: Part I – formulation and discretization. SPE Reservoir Simulation Symposium, Dallas, USA, 8-11 Jun (1997).